Amplitude-Modulated Bursting: A Novel Class of Bursting Rhythms

Theodore Vo, Mark A. Kramer, and Tasso J. Kaper*
Department of Mathematics and Statistics, Boston University, Boston, Massachusetts 02215, USA
(Received 22 April 2016; revised manuscript received 9 September 2016; published 23 December 2016)

We report on the discovery of a novel class of bursting rhythms, called amplitude-modulated bursting (AMB), in a model for intracellular calcium dynamics. We find that these rhythms are robust and exist on open parameter sets. We develop a new mathematical framework with broad applicability to detect, classify, and rigorously analyze AMB. Here we illustrate this framework in the context of AMB in a model of intracellular calcium dynamics. In the process, we discover a novel family of singularities, called toral folded singularities, which are the organizing centers for the amplitude modulation and exist generically in slow-fast systems with two or more slow variables.

DOI: 10.1103/PhysRevLett.117.268101

Bursting—the repeated pattern of closely spaced action potentials separated by quiescence—is a ubiquitous type of neuronal activity, supported by diverse biological and mathematical mechanisms [1–5]. Many different types of bursting have been identified, including square-wave bursting in the pancreas [6], brainstem [7], and cortex [8], elliptic bursting in the basal ganglia [9], thalamic neurons [10], rodent trigeminal neurons [11], and cortex [12], parabolic bursting in the Aplysia abdominal ganglion [13], and many others [4,14]. Although the functional significance of bursting remains incompletely understood, bursts have been proposed to support numerous functional roles. These include the communication of specialized information with more reliability than individual spikes [15,16], synchronization between neuronal populations [17], attention [18], synaptic plasticity [19], and memory and awareness [20].

In this Letter, we report on the discovery of a novel form of bursting, called amplitude-modulated bursting (AMB). The discovery was made for the Politi-Höfer (PH) model [21] for intracellular calcium dynamics. The novel features of AMB are the oscillations in the envelope during the active phase. These oscillations extend the burst duration. Variations in system parameters systematically alter the number of oscillations in the envelope (Fig. 1). Moreover, AMB turns out to be robust.

We also report that the AMB rhythms in the PH model are controlled by torus canard dynamics, and in turn, there is a novel class of singularities for differential equations, which organize the torus canards and hence the AMB. To date, analysis of torus canards has focused on models with only one slow variable [23–26], where torus canards mediate the transition from tonic spiking to bursting of various types. However, these only exist in narrow parameter intervals and are difficult to observe in calcium signalling and in physical systems. By contrast, the PH model has two slow variables, and we find that the torus canards are robust, exist on open parameter sets, and are organized by these novel singularities.

Intracellular calcium dynamics plays a crucial role in the biological function of most cell types. Direct effects include cell depolarization, and indirect effects include modulation of channels permeable to other ions [27], and synaptic transmission. Intracellular calcium encodes information via frequency modulation and amplitude modulation [28], and has also been proposed as central to development and plasticity in the nervous system [29].

The PH model [21] for calcium oscillations due to interactions between calcium transport processes and the metabolism of inositol (1, 4, 5)-trisphosphate (IP_3) is

$$\begin{aligned}
\dot{c} &= J_{\text{release}} - J_{\text{serca}} + \delta(J_{\text{in}} - J_{\text{pm}}),\\
\dot{c}_t &= \delta(J_{\text{in}} - J_{\text{pm}}),\\
\dot{r} &= \frac{1}{\tau_r}\left(1 - r\frac{K_i + c}{K_i}\right),\\
\dot{p} &= k_{3K}\left(V_{PLC} - \frac{c^2}{K_{3K}^2 + c^2}\,p\right).
\end{aligned} \tag{1}$$

Here c and c_t represent the calcium concentration in the cytoplasm and endoplasmic reticulum stores, respectively, r represents the fraction of IP_3 receptors that have not been inactivated by calcium, and p is the concentration of IP_3 in the cytoplasm. The calcium flux through the IP_3 receptors is given by J_{release}; the active transport of calcium across the endoplasmic reticulum and plasma membrane by J_{serca} and J_{pm}, respectively; and the calcium flux into the cell via the plasma membrane by J_{in}. The fluxes J_{release}, J_{serca}, J_{in}, and J_{pm} are functions of (c, c_t, r, p); see [21,22].

The c and r variables evolve rapidly, with time scales of 0.74 s and 6.6 s. The c_t and p variables evolve slowly, with time scales of 200 s and 50 s. That is, the PH model is a slow-fast system with two fast variables (c, r) and two slow variables (c_t, p). The ratio, ε, of fast and slow time scales is proportional to the parameter δ. (In fact, $\varepsilon = 0.0035$ for the δ value given in Fig. 1.) The PH model can be recast in the standard slow-fast form given in [30]; see also [22,31].

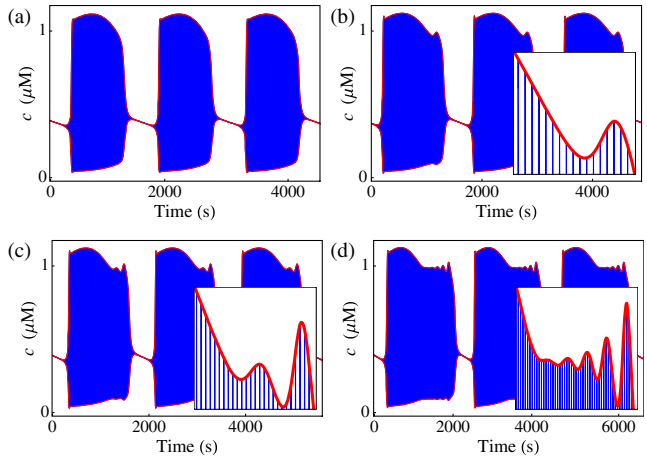

FIG. 1. The PH model (1) exhibits AMB on open parameter sets. Parameter changes switch the system from (a) bursting to (b)–(d) AMB. In (a) $V_{PLC} = 0.151$ μM, (b) $V_{PLC} = 0.1498$ μM, (c) $V_{PLC} = 0.1495$ μM, and (d) $V_{PLC} = 0.1489$ μM. All other parameters are fixed at the values in [22], except $\nu_0 = 0.001$ μMs^{-1} and $\delta \approx 0.473$. The blue curve is the solution of (1), and the red curve is its envelope.

The parameter V_{PLC} represents the steady-state IP_3 concentration in the absence of calcium feedback, and is controlled in experiments [21,22]. Variations in V_{PLC} can generate a wide array of different behaviors. For a range of values including $V_{PLC} = 0.151$ μM, one finds bursts of activity [Fig. 1(a)], which have been classified as subcritical elliptic bursting [4].

A novel type of activity (AMB) is observed for lower values of V_{PLC} [Fig. 1(b)]. The number of oscillations in the envelopes of the bursts increases (Fig. 1, bottom row) as V_{PLC} decreases. Similar behavior is observed on open and physically relevant parameter sets for all other parameters of (1).

In Fig. 2, we address the dynamical mechanisms that govern AMB. The attracting and repelling invariant manifolds, $\mathcal{P}_a^\varepsilon$ and $\mathcal{P}_r^\varepsilon$, of limit cycles are shown in red and blue, respectively, as computed using a novel numerical method [31], which extends existing homotopic continuation methods [25,32]. Each intersection of $\mathcal{P}_a^\varepsilon$ and $\mathcal{P}_r^\varepsilon$ corresponds to a torus canard. The first intersection of $\mathcal{P}_a^\varepsilon$ and $\mathcal{P}_r^\varepsilon$, denoted ξ_0 (black curve), is the strong torus canard. It is the local phase space separatrix that divides between those bursting solutions that exhibit oscillations in their envelope and those that do not. The remaining intersections of the invariant manifolds, ξ_i, $i = 1, 2, 3$ (shown in cyan, brown, and green, respectively), are the secondary torus canards. The innermost intersection of $\mathcal{P}_a^\varepsilon$ and $\mathcal{P}_r^\varepsilon$ is the weak torus canard, ξ_w ($= \xi_4$; black curve). It plays the role of a local axis of rotation; the invariant manifolds and the other torus canards twist around ξ_w.

For each integer $n = 1, 2, \ldots$, families of torus canards are observed on open intervals of V_{PLC}. The secondary torus canards partition the invariant manifolds into

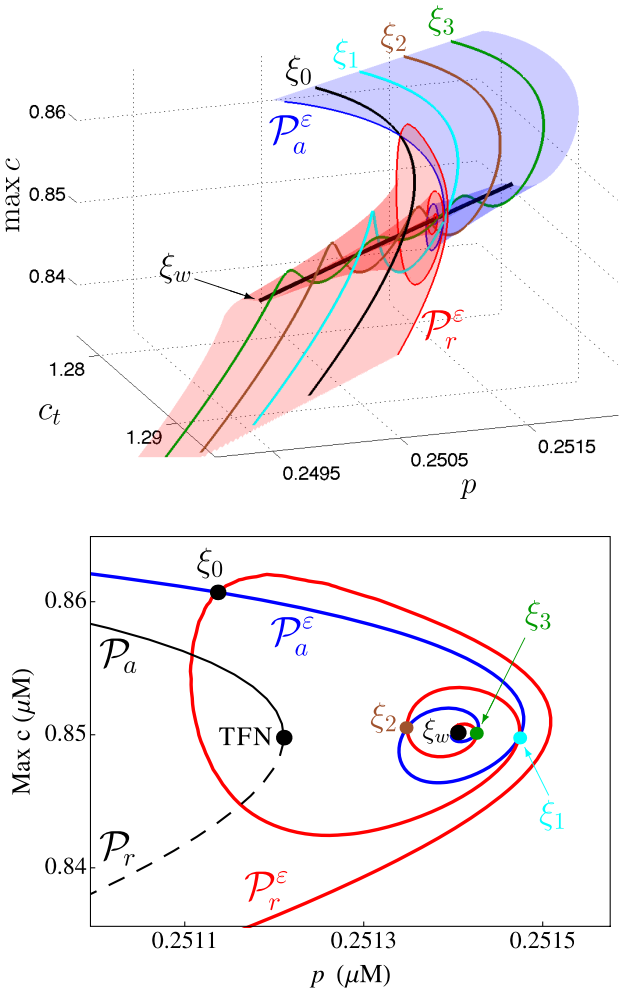

FIG. 2. The invariant manifolds of limit cycles, $\mathcal{P}_a^\varepsilon$ and $\mathcal{P}_r^\varepsilon$, organize the AMB. In the cross section $c_t \approx 1.2844$ (bottom), the attracting and repelling manifolds of limit cycles, $\mathcal{P}_a$ and $\mathcal{P}_r$, of the fast (c, r) subsystem (i.e., for $\varepsilon = 0$) meet at the TFN point. The invariant manifolds, $\mathcal{P}_a^\varepsilon$ and $\mathcal{P}_r^\varepsilon$, for $\varepsilon = 5 \times 10^{-5}$, intersect at the points $\xi_0, \xi_1, \xi_2, \xi_3$, and ξ_w. The torus canard solutions lie in these intersections. Here, $V_{PLC} = 0.2$ μM.

rotational sectors. Every orbit on $\mathcal{P}_a^\varepsilon$ between ξ_{n-1} and ξ_n for $n = 1, 2, \ldots$, is an AMB where the envelope executes n oscillations about ξ_w.

Figure 3 illustrates the rotational sectors formed by the maximal torus canards. For fixed parameters, the number of oscillations in the burst envelope can be changed by adjusting the initial condition. For example, with initial condition on $\mathcal{P}_a^\varepsilon$ between ξ_0 and ξ_1, the trajectory Γ of (1) is an AMB with one oscillation in the envelope (Fig. 3, top row). When the initial condition lies in the sector bounded by ξ_1 and ξ_2 (Fig. 3, middle row), the envelope exhibits two oscillations. Each time the initial condition crosses a torus canard, an extra oscillation is added (Fig. 3, bottom row). By generating extra oscillations in the profile of the AMB, the torus canards reliably increase the burst duration (Fig. 3, right column).

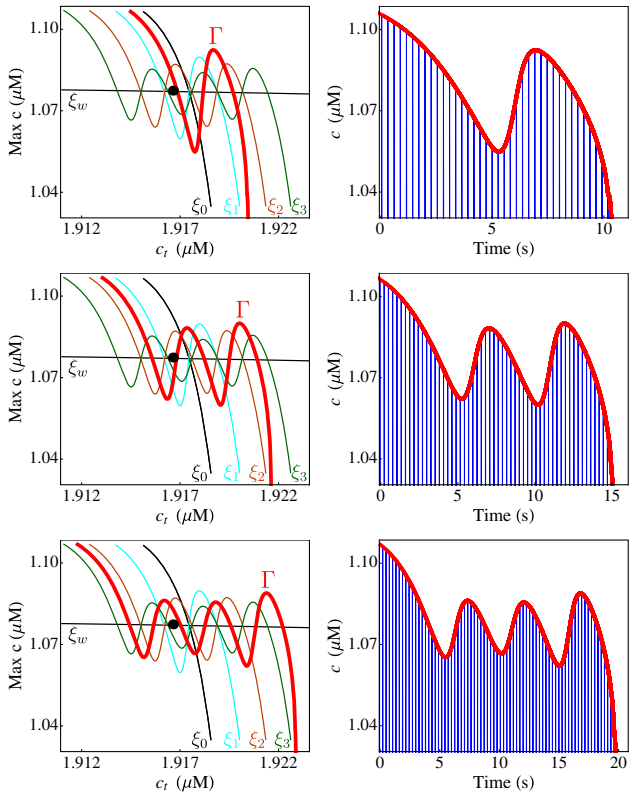

FIG. 3. Transitions through the rotational sectors establish AMBs of different duration. Each torus canard is the boundary between AMB solutions with different numbers of oscillations in the envelope. Parameter values are as in Fig. 1(d). Left column: projection into the (c_t, c) phase space. Four torus canards (ξ_0 to ξ_3) and the weak torus canard (ξ_w) are shown. The black dot indicates the TFN. Right column: time evolution of the AMB solution Γ.

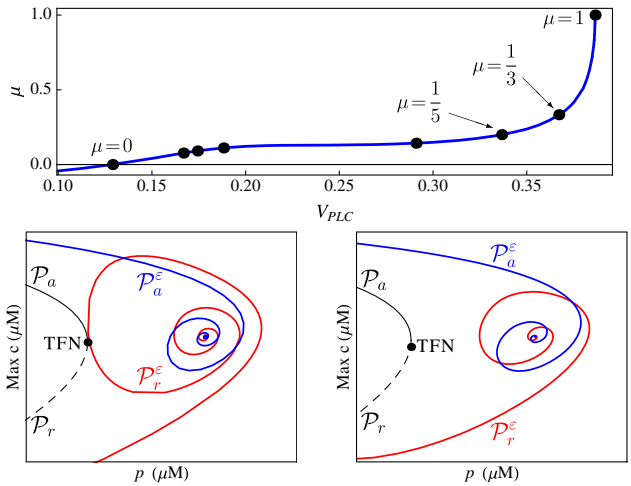

FIG. 4. Top: eigenvalue ratio, μ, of the TFS as a function of V_{PLC}. Black markers indicate odd integer resonances, where secondary torus canards bifurcate from the weak torus canard. Bottom row: cross sections of the invariant manifolds of limit cycles, $\mathcal{P}_a^\varepsilon$ and $\mathcal{P}_r^\varepsilon$, for $\varepsilon = 5 \times 10^{-5}$ in an $\mathcal{O}(\sqrt{\varepsilon})$ neighborhood of the TFN; see Fig. 2. Bottom left: $V_{PLC} = 0.16$ μM and $\mu \approx 0.063\,44$ (2 primary and 7 secondary torus canards). Bottom right: $V_{PLC} = 0.23$ μM and $\mu \approx 0.1297$ (2 primary and 3 secondary torus canards).

The torus canards are the local mechanisms responsible for the amplitude modulation by generating oscillations in the envelope of the bursting waveform. A complete understanding of these dynamics requires determining where the torus canards originate. We find in system (1) that there is a novel family of singularities for differential equations, called toral folded singularities (TFS), from which the torus canards originate. A TFS is a special limit cycle of the fast (c, r) subsystem with two distinguishing features. (i) It is a saddle node of periodics (SNPO). (ii) The averaged slow flow along the manifold, $\mathcal{P}$, of limit cycles of the fast (c, r) subsystem can pass through the TFS with finite, nonzero speed and cross from $\mathcal{P}_a$ to $\mathcal{P}_r$, and follow $\mathcal{P}_r$ for substantial times. This second property distinguishes the TFS from regular SNPOs (where the averaged slow flow along $\mathcal{P}$ blows up in finite time) and is satisfied generically in systems with two or more slow variables.

The eigenvalues at the TFS determine the existence and number of torus canards that persist for ε small and positive. In (1), for $V_{PLC} > 0.386\,42$ μM, the TFS has complex eigenvalues. Hence, they are of focus type, and there are no torus canards. For $0.129\,011$ μM $< V_{PLC} <$ $0.386\,42$ μM (Fig. 4, top row), the TFS has two real negative eigenvalues and is termed a toral folded node (TFN). Torus canards exist on this parameter interval and AMBs are observed. For $V_{PLC} < 0.129\,011$ μM, the TFS has real eigenvalues of opposite sign. Hence, they are of saddle type and have precisely one torus canard. At the transition $V_{PLC} = 0.129\,011$ μM where one of the eigenvalues is zero, the TFS is of saddle-node type. Toral folded saddle nodes mark the boundary between spiking and amplitude modulated rhythms.

The TFNs are the central TFS of interest for AMB. They behave like stable nodes in that all trajectories on $\mathcal{P}_a$ in their basins of attraction will converge to them. The torus canards of a TFN will exist for ε small and positive. With $\mu := \lambda_w/\lambda_s$, where $\lambda_s < \lambda_w < 0$ are the eigenvalues of the TFN, the floor function $\lfloor (\mu + 1)/2\mu \rfloor + 1$ gives the number of torus canards.

In the case of a TFN, each time μ^{-1} increases through an odd integer, an additional secondary torus canard (i.e., an additional oscillation in the envelope of the waveform) appears. Figure 4 (bottom row) illustrates this mechanism in (1). As V_{PLC} decreases and μ^{-1} increases, the invariant manifolds of limit cycles become more twisted, resulting in additional intersections.

Having identified the torus canards and the TFS that are the local mechanisms responsible for the amplitude modulation, we now identify the global return mechanism that completes the AMB rhythm. We begin by constructing the singular attractor, i.e., the orbit that the system converges to in the limit $\varepsilon \to 0$ (Fig. 5, black trajectory). The singular

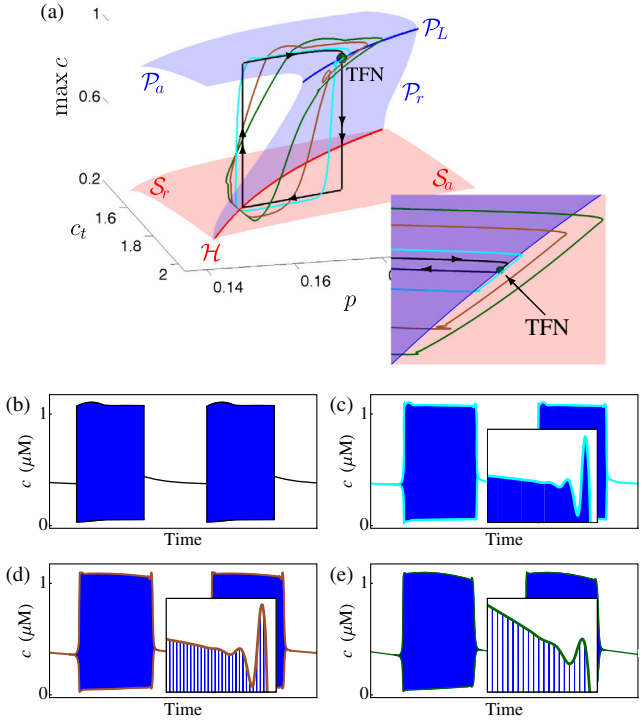

FIG. 5. The AMB rhythm consists of a local mechanism of amplitude modulation and a global return mechanism. (a) Geometric construction of the AMB rhythm. The critical manifold (red surface), $\mathcal{S}_a \cup \mathcal{S}_r$, possesses a curve of Hopf bifurcations $\mathcal{H}$ of the fast subsystem. The manifold of limit cycles (blue surface), $\mathcal{P}_a \cup \mathcal{P}_L \cup \mathcal{P}_r$, emanates from $\mathcal{H}$. The colored trajectories are the ε-unfoldings of the singular attractor for $\varepsilon = 1 \times 10^{-4}$ (cyan), $\varepsilon = 5 \times 10^{-4}$ (brown), and $\varepsilon = 1 \times 10^{-3}$ (green). The time evolution of the AMB solution is shown for (b) $\varepsilon = 0$, (c) $\varepsilon = 1 \times 10^{-4}$, (d) $\varepsilon = 5 \times 10^{-4}$, and (e) $\varepsilon = 1 \times 10^{-3}$. In each subfigure, the blue curve is the AMB rhythm itself. The envelope color in each subfigure corresponds to the colors in (a).

attractor is the concatenation of four orbit segments. Starting in the quiescent phase, there is a slow drift (black, single arrow) along the attracting equilibria, $\mathcal{S}_a$, of the fast subsystem (i.e., the critical manifold) that takes the orbit up to the curve $\mathcal{H}$ of (subcritical) Hopf bifurcations of the fast subsystem, where the stability of $\mathcal{S}$ changes. This initiates a fast upward transition (black, double arrows) away from $\mathcal{H}$ towards the attracting manifold of limit cycles, $\mathcal{P}_a$. Once the trajectory reaches $\mathcal{P}_a$, there is an average slow drift (black, single arrow) that moves the orbit along $\mathcal{P}_a$ towards the SNPO, labeled $\mathcal{P}_L$, and into the basin of attraction of the TFN. The slow drift brings the trajectory to the TFN (green dot), where there is a fast downward transition (black, double arrows) that projects the trajectory to $\mathcal{S}_a$, completing one full cycle of the singular orbit.

Figure 5 shows that the singular attractor perturbs to an AMB rhythm for small ε (colored trajectories). As stated above, the oscillations in the envelope are due to the twisting of the invariant manifolds of limit cycles in the neighborhood of the TFN. The size of the oscillations in the envelope varies with ε. First, the invariant manifolds of limit cycles spiral around the weak torus canard with amplitude $\mathcal{O}(\sqrt{\varepsilon})$. [Thus, the amplitude of the modulations is $\mathcal{O}(\sqrt{\varepsilon})$.] Second, the position of the AMB trajectory changes relative to the maximal torus canards as ε increases; the cyan and brown trajectories in Fig. 5 are closer to one of the maximal torus canards than the green trajectory. The green solution lies in a different rotational sector than the cyan and brown solutions. Hence, the green solution has fewer oscillations.

Eventually, the trajectory leaves the neighborhood of the TFN and enters the silent phase of the burst. The silent phase is a small $\mathcal{O}(\varepsilon)$-perturbation of the slow drift on $\mathcal{S}_a$. The trajectory does not immediately leave the silent phase when it reaches $\mathcal{H}$. Instead, the initial exponential contraction along $\mathcal{S}_a$ allows trajectories to follow the repelling slow manifold, $\mathcal{S}_r$, to the left of $\mathcal{H}$ for substantial times [33]. However, there eventually comes a moment where the repulsion on $\mathcal{S}_r$ overwhelms the accumulated contraction and the trajectory transitions to be near $\mathcal{P}_a$. This returns the trajectory to one of the rotational sectors formed by the maximal torus canards, and completes the AMB cycle.

The interburst frequency is determined by the amount of time the trajectory spends in the silent phase. To leading order (for $\varepsilon = 0$), this is the time taken for the orbit to move from where it lands on $\mathcal{S}_a$ to where it encounters $\mathcal{H}$. For ε small and positive, the interburst frequency changes slightly each time the AMB returns to the silent phase.

In summary, we have reported on the existence of novel amplitude-modulated bursting (AMB) solutions in the PH model (1) for intracellular calcium dynamics and found that they originate from a combination of local and global mechanisms. The local mechanism consists of the toral folded nodes (TFN), which control the number of oscillations in the burst envelope and organize the attendant torus canards. The global mechanism funnels orbits into the rotational sectors of the TFN.

Motivated by this discovery of the AMB and the TFN in (1), we developed a new mathematical framework in [31] for TFN, torus canards, and AMB solutions in slow-fast systems with two (or more) slow variables. This theory shows that the TFN, torus canards, and AMB solutions are generic, so that they exist robustly in neuroscience, including the Hindmarsh-Rose [34], Morris-Lecar-Terman [35], and Wilson-Cowan-Izhikevich [4] models, as shown in [31]. Also, connections are made in [31] to torus canards in the forced van der Pol equation [25], which is a prototypical nonlinear oscillator in biology, electrical engineering, and physics. Moreover, the numerical study of [36] shows that generic torus canards also exist in a model of coupled respiratory neurons in the pre-Bötzinger complex.

The robustness of the torus canards in these models indicates that it may be possible to observe AMB experimentally. While no direct examples have been found yet, a possible example of AMB in experimental recordings can

be found in leech heart interneurons [37,38]. The time series reported in [39] from a model of leech heart exhibits a rhythm generated by local mechanisms that appears to be somewhat similar to AMB.

AMB solutions represent a form of combined amplitude and frequency modulation (AM, FM). The oscillations in the burst amplitude introduce a second, lower frequency modulating the high-frequency fast oscillations, while at the same time the envelope of the burst exhibits AM. As shown in [28], both AM and FM are crucial to intracellular calcium signalling. The potential of combined AM and FM may also be of significance in communication and laser technology.

Finally, we observe that our study of the PH model has also identified the entire class of toral folded singularities (TFS) to which the TFN belong. The other types of TFS, which are presented in [31] have different types of torus canard dynamics associated with them. Hence, there is the potential for discovering further novel solutions.

The research of T. V. and T. J. K. was partially supported by NSF-DMS 1109587. M. A. K. was partially supported by the NSF CAREER Grant No. NSF-DMS 1451384. T. V. and M. A. K. were partially supported by a Career Award at the Scientific Interface from the Burroughs Wellcome Fund.

*tasso@math.bu.edu

[1] J. Rinzel, in *Mathematical Topics in Population Biology, Morphogenesis, and Neurosciences*, Lecture Notes in Biomathematics Vol. 71, edited by E. Teramoto and M. Yamaguti (Springer-Verlag, Berlin, 1987), pp. 267–281.
[2] R. Bertram, M. J. Butte, T. Kiemel, and A. Sherman, Bull. Math. Biol. **57**, 413 (1995).
[3] R. Krahe and F. Gabbiani, Nat. Rev. Neurosci. **5**, 13 (2004).
[4] E. Izhikevich, Int. J. Bifurcation Chaos Appl. Sci. Eng. **10**, 1171 (2000).
[5] E. M. Izhikevich, Scholarpedia **1**, 1300 (2006).
[6] R. Bertram, P. Smolen, A. Sherman, D. Mears, I. Atwater, F. Martin, and B. Soria, Biophys. J. **68**, 2323 (1995).
[7] R. J. Butera, J. Rinzel, and J. C. Smith, J. Neurophysiol. **82**, 382 (1999).
[8] A. Kepecs and X.-J. Wang, Neurocomputing **32–33**, 181 (2000).
[9] G. Lajoie and E. Shea-Brown, SIAM J. Appl. Dyn. Syst. **10**, 1232 (2011).
[10] A. Destexhe, D. A. McCormick, and T. J. Sejnowski, Biophys. J. **65**, 2473 (1993).
[11] C. D. Negro, C. F. Hsiao, S. H. Chandler, and A. Garfinkel, Biophys. J. **75**, 174 (1998).
[12] X.-J. Wang, NeuroReport **5**, 221 (1993).
[13] J. Rinzel and Y. S. Lee, J. Math. Biol. **25**, 653 (1987).
[14] G. B. Ermentrout and D. H. Terman, *Mathematical Foundations of Neuroscience* (Springer, New York, 2010).
[15] F. Gabbiani, W. Metzner, R. Wessel, and C. Koch, Nature (London) **384**, 564 (1996).
[16] J. E. Lisman, Trends Neurosci. **20**, 38 (1997).
[17] R. D. Traub, M. A. Whittington, I. M. Stanford, and J. G. Jefferys, Nature (London) **383**, 621 (1996).
[18] F. Crick, Proc. Natl. Acad. Sci. U.S.A. **81**, 4586 (1984).
[19] L. F. Abbott and W. G. Regehr, Nature (London) **431**, 796 (2004).
[20] C. Koch and F. Crick, in *Large-Scale Neuronal Theories of the Brain*, edited by C. Koch and J. Davis (MIT Press, Cambridge, 1994), pp. 93–110.
[21] A. Politi, L. D. Gaspers, A. P. Thomas, and T. Hofer, Biophys. J. **90**, 3120 (2006).
[22] E. Harvey, V. Kirk, M. Wechselberger, and J. Sneyd, J. Nonlinear Sci. **21**, 639 (2011).
[23] G. N. Benes, A. M. Barry, T. J. Kaper, M. A. Kramer, and J. Burke, Chaos **21**, 023131 (2011).
[24] J. Burke, M. Desroches, A. M. Barry, T. J. Kaper, and M. A. Kramer, J. Math. Neurosci. **2**, 3 (2012).
[25] J. Burke, M. Desroches, A. Granados, T. J. Kaper, M. Krupa, and T. Vo, J. Nonlinear Sci. **26**, 405 (2016).
[26] M. A. Kramer, R. D. Traub, and N. J. Kopell, Phys. Rev. Lett. **101**, 068103 (2008).
[27] R. D. Traub, J. G. Jefferys, R. Miles, M. A. Whittington, and K. Tóth, J. Physiol. **481**, 79 (1994).
[28] M. De Pittá, V. Volman, H. Levine, G. Pioggia, D. DeRossi, and E. Ben-Jacob, Phys. Rev. E **77**, 030903 (2008).
[29] A. Ghosh and M. E. Greenberg, Science **268**, 239 (1995).
[30] $\dot{c} = f_1 + \varepsilon g_1$, $\dot{r} = f_2$, $\dot{c}_t = \varepsilon g_1$, $\dot{p} = \varepsilon g_2$, where f_i, g_i are functions of (c, r, c_t, p) for $i = 1, 2$.
[31] T. Vo, arXiv:1606.02366.
[32] M. Desroches, B. Krauskopf, and H. M. Osinga, SIAM J. Appl. Dyn. Syst. **7**, 1131 (2008).
[33] A. I. Neishtadt, Differ. Equ. **23**, 1385 (1987).
[34] K. Tsaneva-Atanasova, H. M. Osinga, and A. Sherman, J. Theor. Biol. **264**, 1133 (2010).
[35] D. Terman, SIAM J. Appl. Math. **51**, 1418 (1991).
[36] K.-L. Roberts, J. Rubin, and M. Wechselberger, SIAM J. Appl. Dyn. Syst. **14**, 1808 (2015).
[37] G. S. Cymbalyuk, Q. Gaudry, M. A. Masino, and R. L. Calabrese, J. Neurosci. **22**, 10580 (2002).
[38] A.-E. Tobin and R. L. Calabrese, J. Neurophysiol. **94**, 3938 (2005).
[39] A. A. Hill, M. A. Masino, and R. L. Calabrese, J. Neurophysiol. **87**, 1586 (2002).